Pollutant Dissipation at the Sediment-Water Interface: A Robust Discrete Continuum Numerical Model and Recirculating Laboratory Experiments

Guillaume Drouin, Marwan Fahs, Boris Droz, Anis Younes, Gwenael Imfeld, Sylvain Payraudeau

Water Resources Research

RESEARCH ARTICLE
10.1029/2020WR028932

Pollutant Dissipation at the Sediment-Water Interface: A Robust Discrete Continuum Numerical Model and Recirculating Laboratory Experiments

Guillaume Drouin[1], Marwan Fahs[1], Boris Droz[1], Anis Younes[1], Gwenaël Imfeld[1], and Sylvain Payraudeau[1]

[1]CNRS, ENGEES, ITES UMR 7063, University of Strasbourg, Strasbourg, France

Key Points:

- An advanced flow and reactive transport model is developed to simulate pollutant dissipation at the sediment-water interface
- A new laboratory setup for bench-scale tracer experiment is developed and methodology of model calibration is provided
- Bedforms and vertical velocities play a crucial role in the mass exchange at the sediment-water interface

Supporting Information:

- Supporting Information S1

Correspondence to:

M. Fahs and S. Payraudeau,
fahs@unistra.fr;
sylvain.payraudeau@engees.unistra.fr

Citation:

Drouin, G., Fahs, M., Droz, B., Younes, A., Imfeld, G., & Payraudeau, S. (2021). Pollutant dissipation at the sediment-water-interface: A robust discrete continuum numerical model and recirculating laboratory experiments. *Water Resources Research*, *57*, e2020WR028932. https://doi.org/10.1029/2020WR028932

Received 4 OCT 2020
Accepted 12 JAN 2021

Abstract Pollutant exchange in the hyporheic zone is a major process controlling its degradation in river systems. Knowledge of mass transfer processes at the sediment-water interface (SWI) remains scarce. Accurate predictive modeling of flow driving pollutant fluxes at the SWI is currently limited. We examined mass exchange at the SWI by combining laboratory tracer experiments and the development of a flow reactive transport (FRT) model. NaCl and Foron Blue 291 tracers were used as surrogates of conservative and moderately sorptive organic pollutants, respectively. Tracer experiments in the bench-scale river channel reproduced the influence of overlying water velocities, the source of the pollutant, and its sorption capacity on pollutant exchange. A methodological framework to calibrate the FRT model against experiments was developed. Good agreement between the experimental and numerical results confirmed the robustness of the experimental setup and numerical model. The pollutant origin, either from the sediment or the overlying water, did not affect the pollutant exchange rates. The exchange rates were quasi-proportional to the overlying water velocity. The sediment bed caused retention of more than half of the initially injected mass of Foron Blue 291. The moderately sorptive tracer partitioning retarded the equilibrium up to six times compared with the conservative tracer NaCl. Numerical tests, including both overlying and vertical velocities, showed that the latter is the main factor controlling pollutant exchange at the SWI. Altogether, the model allows capturing interactions between pollutant transport and partitioning to the rivers sediment, paving the way for systematic investigations of pollutant behavior in rivers.

1. Introduction

More than one-third of globally available freshwater resources is used for human activities, and freshwater pollutions by macro- and micro-pollutants are recurring and widespread (Sousa et al., 2018). Rivers are the most sensitive environmental compartments to pollution hazards, especially low Strahler order rivers, which may receive proportionally larger loads of pollutants relative to their water discharge (Honti et al., 2018; Munz et al., 2011). Hyporheic zone processes in rivers affect both biogeochemical activities and pollutant mixing in the sediment bed (Boano et al., 2014). Despite decades of intense research on the hyporheic zone, the dynamics of hyporheic zone processes remain partly unresolved. In particular, current approaches often fail to identify and hierarchize the predominant factors controlling interactions between pollutants and river sediment beds in the hyporheic zone.

Hyporheic processes controlling pollutant transformation mainly occur at the sediment-water interface (SWI) where dissolved species (e.g., organic matter, nitrates, oxygen, etc.) from the overlying water or the groundwater mix within the riverbed sediment, resulting in various redox gradients, themselves controlling the pollutant fate in rivers (Byrne et al., 2014). Hydrological conditions in rivers, including the succession of low flow and flooding events, vertical surface-groundwater exchanges, and geomorphological variations of river reaches, affect the transport of dissolved pollutants at the SWI (Briggs et al., 2014; Dwivedi et al., 2018; Lansdown et al., 2015). In addition, the propensity of a pollutant to sorb and degrade within the sediment bed controls its accumulation in the hyporheic zone (Liao et al., 2013). Sorption typically increases the pollutant mean residence time in the sediment bed and alters its distribution across the hyporheic zone (Ren & Packman, 2004a, 2004b). Hence, the interplay between hydraulic processes and pollutant partitioning at the SWI currently limits our understanding of pollutant fate in river systems (Krause et al., 2017).

In this context, the characterization of hyporheic exchanges in rivers can rely on laboratory tracer experiments (Liao et al., 2013). Tracers can be used as surrogates of pollutants that may facilitate investigations of

pollutant fate at the SWI. The experimental procedures generally involve intense logistics, including technical constraints and space, and may be expensive (Table S1). Chandler et al. (2016) and Fox et al. (2014) examined the effect of hydraulic forcing variation on tracer exchange at the SWI. Previous research has focused on the effects of riverbed geometries (Cardenas & Wilson, 2007b) and pollutant physicochemical properties on the mass flux at the SWI (Ren & Packman, 2004b). While previous studies often relied on large-scale experimental setups (~m), small-scale experiments (~cm) in recirculating flumes also demonstrated to be promising to study water flow, and sediment transport in rivers, as they allow for repetitive testing (Malverti et al., 2008).

Although adapted experimental flumes can be designed, characterizing the processes governing pollutant transport at the SWI remains delicate because the direct observation of velocity fields in the sediment bed is often limited. In this context, conceptual and physically based reactive transport modeling can help to characterize and interpret transport processes in the sediment bed (Voermans et al., 2017). Conceptual diffusive models rely on Fick's law with an effective diffusivity featuring the combined effect of diffusion, hydrodynamic dispersion, and small-scale advective processes. While diffusive models are computationally inexpensive to simulate pollutant mass exchange at the SWI (Voermans et al., 2018), they rely on systematic and site-specific experimental characterizations of the effective diffusivity. These characterizations severely limit the extrapolation of diffusive models to different river conditions. On the other hand, physically based flow-reactive-transport (FRT) models couple operators representing flow, pollutant transport, and reactive processes across the SWI (Angot et al., 2017; Kaufman et al., 2017). FRT models intrinsically overcome the limitations of the diffusive models and allow a more generic representation of pollutant exchange at the SWI. For instance, recently, Liu et al. (2020) performed 3D numerical simulations to understand the effect of sediment heterogeneity on the hyporheic exchange and solute transport along the SWI. One major drawback of FRT models is, however, the lack of accurate simulations of flows at the SWI.

In several existing models, Darcy's law is used for both fluid and porous regions. Fluid flow in the fluid region is approximated with the Darcy's law with high permeability. This allows for ensuring the continuity of primary variables and results in a consistent mathematical system. However, the velocity in the fluid layer, as well as in layers of highly permeable sediment, cannot be accurately simulated with the Darcy's model (Salim Joodi et al., 2010; Xu et al., 2018). The classical approach, that uses the Navier-Stokes equation within the overlying water and the Darcy's equation within the porous sediment bed, leads to a more robust representation of flows but requires coupling the conservation equations at the interface using appropriate boundary conditions (Ehrhardt, 2012) because the continuity of normal and tangential velocities, stress and pressure at the interface cannot be simultaneously ensured. This challenges the selection of the most suited interface conditions and makes it case-specific (Bars & Worster, 2006; Lācis & Bagheri, 2017; Valdés-Parada et al., 2013).

The purpose of this study is thus to improve the mechanistic interpretation of pollutant exchange at the SWI in rivers. We developed a novel FRT model based on the combination of Navier-Stokes and Brinkman models, for the fluid (i.e., overlying water) and the porous region (i.e., sediment bed), respectively, and a recirculating laboratory bench-scale tracer experiment at the SWI. The FRT model relies on numerical schemes continuously solving the governing flow and pollutant transport equations for both the fluid and porous regions. The bench-scale river channel enables repetitive tests under a large panel of hydraulic conditions and allows NaCl and Foron Blue 291 (FB291) tracers to be used as surrogates of conservative and moderately sorptive organic pollutants, respectively. We present a methodology to calibrate the numerical model against experimental data to evaluate the suitability of the new numerical model and the experimental device. Finally, we investigate numerically the impact of losing and gaining rivers on pollutant exchange at the river scale, which paves the way for future studies of pollutant reactive transport in river systems.

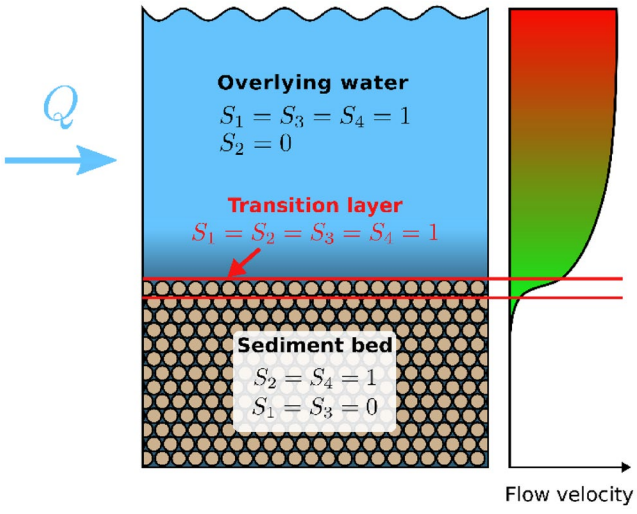

Figure 1. Conceptual description of the domain decomposition with parameters used in Equation 1 for the three layers configuration.

2. The FRT Numerical Model

The novelty of the conceptualization and the resolution of the physically based discrete continuum FRT model presented here lies in the continuity of all state variables at the fluid-porous interface, that is, between the overlying water and the riverbed sediment (Figure 1). This

continuity allows the generic resolution of pollutant transport at the SWI under various hydrological conditions.

2.1. Fundamental Equations

The Navier-Stokes and Brinkman equations were merged into a single equation (Equations 1 and 2). The set of logical coefficients (s_1, s_2, s_3, s_4) was used to switch from the fluid to the high and low permeable porous domains in the sediment layer as depicted in Figure 1. The continuity of all variables was thus ensured while empirical interfacial conditions were not necessary to compute the flow or transport as it would be with classical multidomain approaches (Bars & Worster, 2006; Tian & Wang, 2017, 2018; Yadav et al., 2017).

$$s_1 \cdot \frac{\rho}{\epsilon} \cdot \frac{\partial \boldsymbol{u}}{\partial t} + s_2 \cdot \frac{\mu}{K} \cdot \boldsymbol{u} + s_3 \cdot \frac{\rho}{\epsilon^2} \cdot \left(\boldsymbol{u} \cdot \nabla\right) \cdot \boldsymbol{u} - s_4 \cdot \frac{\mu}{\epsilon} \cdot \nabla \cdot \left(\nabla \boldsymbol{u}\right) + \nabla \mathrm{P} = -\rho \cdot g \cdot \nabla z \tag{1}$$

$$\nabla \cdot \boldsymbol{u} = 0 \tag{2}$$

where $\boldsymbol{u}$ $[\boldsymbol{L}/\boldsymbol{T}]$ is the fluid velocity, including horizontal and vertical components, and P is the water pressure $[M/L/T^2]$. ρ and μ are the water volumetric mass density $[M/L^3]$ and the dynamic viscosity $[M/L/T]$, ϵ is the sediment porosity, g is the gravity $[L\ /\ T^2]$, and z is the vertical position $[L]$. The coefficient s_1, s_2, s_3, and s_4 can be set as 0 or 1, which allows for switching automatically between full Navier-Stokes equation, Darcy-Brinkman model, or Darcy's law.

In the overlying water, the flow was described using the Navier-Stokes equations by setting coefficients s_1, s_3, and s_4 to be 1 and coefficient s_2 to be 0. In the porous medium of low permeability (i.e., sediment bed layer), Darcy's law was applied by suppressing the transient effect and the convective term of the Brinkman equation, corresponding to s_1, s_3, and s_4 equal to 0 and s_2 equal to 1. A transition layer with a high permeability was introduced between the fluid and the porous region. The occurrence of a transition layer at the fluid-porous interface (Nield, 1983) has been experimentally validated previously (Goharzadeh et al., 2005). The thickness of the transition layer was in the same size order as the grain size of the porous medium. In this transition layer, all coefficients of the Brinkman equation were set to 1.

The FRT model is based on the advection-dispersion-reaction equations (Equations 3 and 4):

$$\epsilon \cdot \frac{\partial \mathrm{C_i}}{\partial t} + \rho_{\mathrm{bulk}} \cdot \frac{\partial S_i}{\partial t} + \boldsymbol{u} \cdot \nabla C_i - \nabla \cdot \left(\boldsymbol{D_i} \cdot \nabla C_i\right) = \boldsymbol{r_i} \tag{3}$$

$$\boldsymbol{D_i} = D_{m,i} \cdot \boldsymbol{I} + \boldsymbol{D}_{\mathrm{disp}} = \left(\alpha_T \cdot |\boldsymbol{u}| + D_m\right) \cdot \delta_{lm} + \left(\alpha_L - \alpha_T\right) \cdot \frac{u_l \cdot u_m}{|\boldsymbol{u}|} \quad l, m = 1, 2 \tag{4}$$

where C_i $[M/L^3]$ represents the dissolved pollutant concentration, subscript i indicates the chemical species i, S_i $[M/M]$ is the sorbed concentration, ρ_{bulk} is the bulk density of the porous medium $[M/L^3]$, $\boldsymbol{D_i}$ is the related dispersion tensor $[L^2/T]$ accounting for pollutant molecular diffusion ($D_{m,i}$) $[L^2/T]$, and longitudinal (α_L) and transversal (α_T) dispersion $[L]$, δ_{lm} is the Kronecker function, and r_i is the reactive term representing degradation of species i.

The model application was limited in our case to laminar flow, although the proposed approach can be extended to turbulent flow. While turbulent flow in the overlying water may enhance mass exchange at the SWI (Grant & Marusic, 2011), turbulences are not expected to penetrate in the sediment bed except under conditions of high velocities, and/or very coarse and permeable sediment (Boano et al., 2014; Voermans et al., 2017). The model application to laminar flow is justified here by the predominance of low Strahler order rivers (<2) accounting for 75% of the global river length (Downing, 2012). The limited velocity in low Strahler order rivers favors laminar flow, except during floods, and sediment bed clogging even from coarse sand riverbed (Jin et al., 2019), which limits turbulent flow penetration into the sediment bed. The model is thus valid below the critical Reynolds number. This number is generally observed around $Re = 3{,}000$ (Suga et al., 2010) and can theoretically even reach $Re = 15{,}000$ when sediment bed permeability decreases (Sparrow et al., 1973).

Kinetic sorption was also considered because the residence times of pollutants at the SWI range from minutes up to days (Liao et al., 2013). A one site reversible sorption was adopted, as previously recommended in sorption studies involving metal ions and quartz sand sediment bed (Eylers et al., 1995). Adsorption and desorption were thus implemented with the one-site first order kinetic sorption described in van Genuchten and Wagenet (1989). The sorption isotherm followed a reversible linear relationship (Equation 5). Sorption equilibrium was assumed to be fully established within 12 h (OECD, 2000).

$$\frac{\partial S_i}{\partial t} = \alpha_i \cdot \left(K_{d,i} \cdot C_i - S_i\right) \tag{5}$$

where $K_{d,i}$ is the phase partitioning coefficient of species i in $[L^3/M]$ and α_i is the first-order rate of adsorption $[T^{-1}]$.

2.2. Numerical Resolution

The equations were solved using appropriate numerical techniques for space discretization and time integration. Specific numerical methods were implemented for flow, advection, diffusion-dispersion, and reaction operators to obtain efficient simulations (in terms of computation time) while maintaining high accuracy and continuity of the state variables and mass fluxes between the water and sediment layers. The developed model relies on the numerical scheme suggested by Younes et al. (2014) to solve the coupled Navier-Stokes and heat transfer equations (Younes et al., 2014). The same numerical scheme was adopted here to solve the merged form of Navier-Stokes and Brinkman model (Equation 1) coupled with the mass transport equations of the reactive system (Equation 3). Flow, transport, and reactive operators were sequentially solved. The flow equation was solved with the nonconforming Crouzeix-Raviart (CR) finite element method (Burman & Hansbo, 2005). In contrast to the standard conforming finite element method, the nonconforming method deals with velocities at the edges of elements of the computational mesh. This important property ensures local mass conservation and yields continuous fluxes at the SWI without any specific treatment.

Solving the advection dominated transport is challenging. Standard Eulerian methods are known to introduce unphysical oscillations or numerical diffusion. Avoiding these numerical artifacts requires dense computational grids and small time steps that lead to impractical computation times. We used here the discontinuous-Galerkin (DG) finite element method (Miller et al., 2013) to overcome these difficulties and discretize the advection term of the transport equation. The DG method is superior to existing finite element methods (Miller et al., 2013). In contrast to the standard finite element method, the DG method deals with discontinuous representation of the solution allowing for handling sharp fronts. DG is suitable for our specific SWI application because it can be accurately coupled with the CR finite element method and captures sharp fronts of concentrations caused by physical discontinuities (e.g., permeability gradient at the SWI). The diffusion-dispersion term of the transport equation was discretized using the point flux approximation (MPFA) method. This method was selected because of its local mass conservation property. Further, MPFA was condensed in a single system with the DG method to avoid splitting errors when solving advection and diffusion-dispersion terms separately (Younes et al., 2014). The operator splitting approach was used to include the reactive term. With this approach, the results of the transport operator are used as initial values to update species concentrations based on chemical reactivity. The kinetic reactive transport was solved using the backward differentiation formula (Fahs et al., 2011).

An adaptive, noniterative time stepping was used for time integration to ensure numerical model accuracy and performance (Hirthe & Graf, 2012). This technique adapts the time step during simulation from an estimation of the local truncation error due to time discretization. The time stepping procedure also controls intrinsic error caused by the operator splitting approach when dealing with chemical reactions (Fahs et al., 2008).

The developed numerical scheme combining previously described methods was validated against Fourier series solutions for problems of free fluids (Navier-Stokes equation) in Fahs and Younes (2014). The correctness of the developed code was further checked by comparison with COMSOL® multiphysics for cases including either pure Darcy or Brinkman model (results not shown).

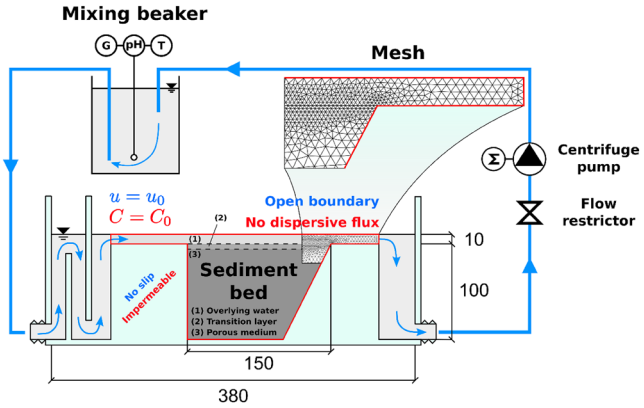

Figure 2. Bench-scale river channel setup. Quotations are in mm. Water was recirculated over the sediment bed with a centrifuge pump. A mixing beaker was placed in the circulating loop to measure tracer concentrations, pH, temperature (T), and conductivity (G). A flow restrictor controlled the water height within the channel. Water flow was controlled by the height difference between the channel and the mixing beaker. The computational domain is delineated by red lines. Boundary conditions are shown in blue for flow (no slip or open boundary) and in red for mass transport (impermeable or no dispersive flux). An example of extracted computational mesh is represented with smaller elements at the SWI interface.

3. Tracer Recirculation in Bench-Scale River Channel

The experimental laboratory bench-scale river channel allowed examining the relationship between hydrological conditions and the transport of tracers as surrogates of pollutants at the SWI.

3.1. Experimental Setup

The tracer experiments were conducted in a closed and recirculated bench-scale river channel (Figure 2). The recirculated system allows studying dissolved pollutant transport as it mimics long river reaches (>km) in a space as limited as a laboratory bench (<30 cm) while running with a constant water volume (≈2L).

The bench-scale river channel was made of glass and composed of a channel and a mixing beaker (Figure 2). All materials were selected to limit organic tracers and pollutant sorption. The sediment bed defining the SWI was 15 cm long (L_{sb}) and centered around a 28 cm long channel allowing flow stabilization along the interface. Water was pumped by a centrifuge pump (Iwaki MD-15R) through Isoversinic® tubing (diameter = 10 mm) at the outlet up to the mixing beaker and fed back by gravity to the channel. Flow restrictors at the inlet of the pump and of the channel allowed setting the water flow and water height constant over time. The sand bed was 10 cm deep and made of thoroughly washed homogeneous sand (Kaltenhouse K30—France, $\phi_{50} = 493\ \mu$m, $\phi_{95} = 786\ \mu$m, detailed composition in Text S1). The sand porosity ($\epsilon = 0.35 \pm 0.01$) did not change across experiments. The sediment apparent density ($\rho_{bulk} = 1{,}700\ \text{kg}\cdot\text{m}^{-3}$) was determined from the sand density provided by the manufacturer. A mean sand saturated conductivity of $K_0 = 7.4 \pm 2.2\cdot10^{-4}\ \text{m}\cdot\text{s}^{-1}$ was determined from six replicates using the constant-head method.

3.2. Conservative and Sorptive Tracer Experiments

Tracer experiments were carried out to study the relationship between water flow, pollutant transport, and sorption patterns at the SWI. Two configurations have been investigated with either pollutant originating from the sediment or the overlying water. Saline solution (NaCl) was used as a pollutant for the conservative tracer and the dye FB291 (CAS Number: 56548-64-2) was used as a strongly sorptive molecule (Berez et al., 2016). The combination of tracers with different sorptive properties allowed to distinguish between organic pollutant transport and phase partitioning in lab-scale constructed wetlands (Fernandez-Pascual et al., 2020). The initial salt concentrations were adjusted to prevent density-driven flow during mixing with NaCl (500 $\text{mg}\cdot\text{L}^{-1}$) (Nagaoka & Ohgaki, 1990) or to avoid precipitation of FB291 (150 $\text{mg}\cdot\text{L}^{-1}$). The tracers were injected in ultrapure water ($\Omega > 15$ MOhm) alone for NaCl and with 0.01 M $CaCl_2$ for FB291 to obtain a typical solution ionic strength (OECD, 2000). The pH remained constant at 7.0 ± 0.5 across the experiment. Twenty-four hours of equilibration were conducted after the addition of the saline solutions to the sediment to ensure establishment of sorption equilibrium with FB291. The tracer experiments lasted between 1 and 12 days and ended when no significant variation of salt concentrations was observed in the mixing beaker or the sediment bed.

The adsorption properties of FB291 were derived from the batch adsorption equilibrium method (OECD, 2000) (Text S2), which was used previously in similar experiments (Eylers et al., 1995; Ren & Packman, 2004a). The linear sorption isotherm was most suited for FB291, yielding a $K_d = 7.7 \pm 0.2\ \text{mL}\cdot\text{g}^{-1}$. The sorption of FB291 on sand occurs by electrostatic interaction forces between the cationic form of the organic pollutant and the negatively charged surface of quartz at experimental pH = 7.5 ± 0.5 (Jada & Ait Akbour, 2014). A reversible adsorption/desorption process with no hysteresis (i.e., no significant nonextractable residual fraction and degradation) was thus assumed.

Depending on hyporheic flows, riverbed sediments can alternatively act as a source or a sink of pollutants dissolved in the overlying water (Krause et al., 2017). Cases of pollutant incorporation (I), with the tracer originating from the overlying water (e.g., surface contamination), and solute export (E), with the tracer released from the sediment bed (e.g., groundwater contamination or historical contamination by the river), were examined. In the case of solute incorporation, the sediment bed was filled with ultrapure water, and the tracer was spiked in the mixing beaker. In the case of solute export, the sediment bed was filled with the tracer solution and the mixing beaker was filled with ultrapure water.

The effect of water flow on mass exchange was tested for each case under low (LF) and high flow (HF) conditions. The targeted flow velocities were 1.5 and 5.0 $cm{\cdot}s^{-1}$, corresponding to $Re \approx 100$ and 400 for LF and HF conditions, respectively. The velocities were below the critical Reynolds number for laminar flow and transitional regimes in rectangular open channels (Allen, 1965). The flows were adjusted and water height was kept at 1 cm over the sediment bed. NaCl was used to investigate the effect of solute origin (ILF_{NaCl} vs. ELF_{NaCl} and IHF_{NaCl} vs. EHF_{NaCl}) and the overlying water velocity (ILF_{NaCl} vs. IHF_{NaCl} and EHF_{NaCl} vs. IHF_{NaCl}) on its transport (Table 1). Additional experiments with FB291 were conducted under high flow conditions for incorporation and export cases to investigate the effect of sorption on pollutant transport at the SWI (IHF_{FB291} vs. IHF_{NaCl} and EHF_{FB291} vs. EHF_{NaCl}). Except for the experiments IHF_{FB291} and EHF_{FB291}, the experiment duration was sufficient to establish equilibrium in the first 8 cm of the sediment bed.

3.3. Data Acquisition

The pollutant transport was analyzed from in-bed and overlying water concentration dynamics. The tracer concentrations in the mixing beaker were continuously monitored at a sampling frequency of 30 s. The concentration variations over time within the mixing beaker reflected the global mass exchange. The NaCl concentration was followed-up by conductivity measurements (WTW 350i), converted into concentration with a previously established linear relationship. The FB291 concentration was continuously monitored by a spectrophotometric method (AvaLight-D5 combined with Avaspec204-BL) at $\lambda = 304$ nm, in which the FB291 concentrations showed a strong linear relationship with the absorbance in the range from 1 to 150 $mg{\cdot}L^{-1}$.

The NaCl concentrations in the sediment bed were followed-up by collecting during each experiment 0.8–1 mL of pore water samples every centimeter from a depth of 0.5–7.5 cm with pore water samplers (MicroRhizons®). The sample volumes were adjusted to allow sufficient measurement accuracy while limiting the impact of pore water removal on the experiment. The tracer concentrations were immediately measured. MicroRhizon samplers could not be used for the experiment with FB291 since the tracer sorbed to the samplers. A beaker filled with water, with a similar shape as the mixing beaker, was placed along with the channel and weighed over time to estimate the evaporation. Blank experiments were also conducted for low and high flow without tracer to quantify any unexpected release of ions from the sand which could potentially bias NaCl quantification by conductivity measurements. The raw time-series of tracer concentrations were corrected for evaporation and ions release before comparison with the modeled data (Text S3). The measured concentrations were normalized by the theoretical equilibrium concentration (C_{eq}) to compare the experiments (methodology described in Text S4).

4. Model Validation Versus Experiment

4.1. Numerical Simulations: Conceptual Model, Parameterization, and Domain Discretization

The SWI was split into three areas with distinct physical properties, namely, the overlying water, the transition layer, and the porous medium (see Figure 1). Navier-Stokes was solved in the overlying water, while Brinkman was applied in the transition layer and the porous medium. The size of the transition layer thickness was assumed to correspond to that of the maximum grain diameter ($D_{max} \approx 0.001$ m, Table S1) (Goharzadeh et al., 2005). The porosity of the transition layer (ϵ_{TL}) corresponded to the geometric mean between porosities of the overlying water and the porous medium, giving $\epsilon_{TL} = 0.67$ (Goharzadeh et al., 2005; Voermans et al., 2017). The Carman-Kozeny equation (Equation 6, Carman, 1997) predicted the sediment bed permeability well ($K_0^{CK} = 10.2{\cdot}10^{-4}$ $m{\cdot}s^{-1}$ vs. $K_0 = 7.4 \pm 2.2{\cdot}10^{-4} m{\cdot}s^{-1}$ as measured). The permeability of the transition layer (K_{TL}) was thus assumed to vary accordingly with a fixed $D_{50} = 0.494$ mm.

$$K_{TL} = \frac{\epsilon_{TL}^3}{180 \cdot \left(1 - \epsilon_{TL}\right)^2} \cdot {D_{50}}^2 = 28.7 \cdot K_0 = 2.13 \cdot 10^{-2}\ \mathrm{m \cdot s^{-1}} \quad (6)$$

No-slip boundary conditions were set at the boundary edge except at the inlet and outlet of the channel. Water was forced through the system with an inlet horizontal velocity (Dirichlet condition) and free to flow at the outlet (open boundary). At the free surface, slip condition allowed horizontal but no vertical velocities. Zero flux Neumann boundary conditions were imposed for transport everywhere except at the inlet where the concentrations are imposed. The boundary conditions are also represented in Figure 2. Water recirculation was addressed in the model with an external subroutine actualizing transport boundary conditions for the inlet at each time step.

Model validation was performed sequentially with data from the conservative (i.e., NaCl) and sorptive (i.e., FB291) tracer experiments. Both tracer concentrations were used in the mixing beaker and at different depths of the sediment bed. A simulated confidence interval, computed with the set of parameters $\left(K_0 + \delta_{K_0}; u_x + \delta_{u_x}\right)$ and $\left(K_0 - \delta_{K_0}; u_x - \delta_{u_x}\right)$ as upper and lower limits, accounted for experimental inaccuracies originating from uncertainties in the determination of K_0 and u_x. Here, u_x stands for the horizontal component of the velocity and δ_{u_x} for variations of water velocity due to water height instabilities (±2 mm) during experiments. This methodology revealed the ability of the model to predict mass exchange at the SWI for solutes with distinct physicochemical properties.

The validation procedure minimized the calibration steps. For transport of nonreactive species (i.e., NaCl), the dispersion coefficients were exclusively used as the calibrated parameters as they could not be experimentally determined. Longitudinal and transverse dispersivities were set at $\alpha_L = 0.01$ m and $\alpha_T = \frac{\alpha_L}{10}$ following a manual optimization procedure. The molecular diffusion coefficient for NaCl was set at $D_{\mathrm{NaCl}}\left(25°\mathrm{C}\right) = 1.612 \cdot 10^{-9}\ \mathrm{m^2 \cdot s^{-1}}$ (Harned & Hildreth, 1951). For FB291, no experimental value was found in the literature. Thus, it was set to $D_{\mathrm{FB291}}\left(25°\mathrm{C}\right) = 5 \cdot 10^{-10}\ \mathrm{m^2 \cdot s^{-1}}$ as a reference value for similar azo dyes.

The computational domain was gridded with a triangular mesh with a maximal size of 0.4 cm (5,606 elements in total). A local mesh refinement defined a transition layer between the overlying water and the porous medium (Figure 2). A mesh sensitivity analysis was performed to ensure mesh independency of flow and transport solutions (Text S5).

4.2. Comparing Numerical and Experimental Results

The fit between the observed and modeled results was tested in all conditions with both tracers. $\mathrm{EHF_{NaCl}}$ and $\mathrm{IHF_{FB291}}$ experiments are presented here as representative results.

The model satisfactorily reproduced the dynamics of NaCl concentrations of the $\mathrm{EHF_{NaCl}}$ experiment after calibration of the dispersion coefficients ($\alpha_L = 10^{-2}$ m and $\alpha_T = 10^{-3}\ m$) (Figures 3a and 3b). The observed and simulated mass fluxes through the SWI interface (Φ_O and Φ_M) generally ranged around the identity line (i.e., $\Phi_O = \Phi_M$, Figure 3c), with residual differences close to zero ($\left|\overline{\Delta\Phi}\right| = \left|\overline{\Phi_O - \Phi_M}\right| = 0.10\ \mathrm{mg \cdot h^{-1}}$ and $\sigma_{\Delta\Phi} = 0.79\ \mathrm{mg \cdot h^{-1}}$, Figure 3d).

The modeled sorptive tracer concentrations better fitted with the experimental data than in the case of the modeled NaCl concentrations. The modeled and simulated mass fluxes fitted well after adjustment with a $K_d$value of 3.0 $\mathrm{mL \cdot g^{-1}}$, rather than using the experimental $K_d = 7.7 \pm 0.2\ \mathrm{mL \cdot g^{-1}}$(Figure 4a), ($\left|\overline{\Delta\Phi}\right| = \left|\overline{\Phi_O - \Phi_M}\right| = 0.01\ \mathrm{mg \cdot h^{-1}}$ and $\sigma_{\Delta\Phi} = 0.54\ \mathrm{mg \cdot h^{-1}}$) (Figures 4b and 4c). This observation is consistent with a previous study reporting a sorption coefficient twice lower for the pharmaceutical atenolol in column experiments than in batch sorption experiments (Kiecak et al., 2019). Although in-bed measurements were not possible for experiments with FB291, similar observed and simulated patterns of FB291 penetration into the sediment bed confirmed the validity of simulations in the case of $\mathrm{IHF_{FB291}}$(Figure 6a and 6b).

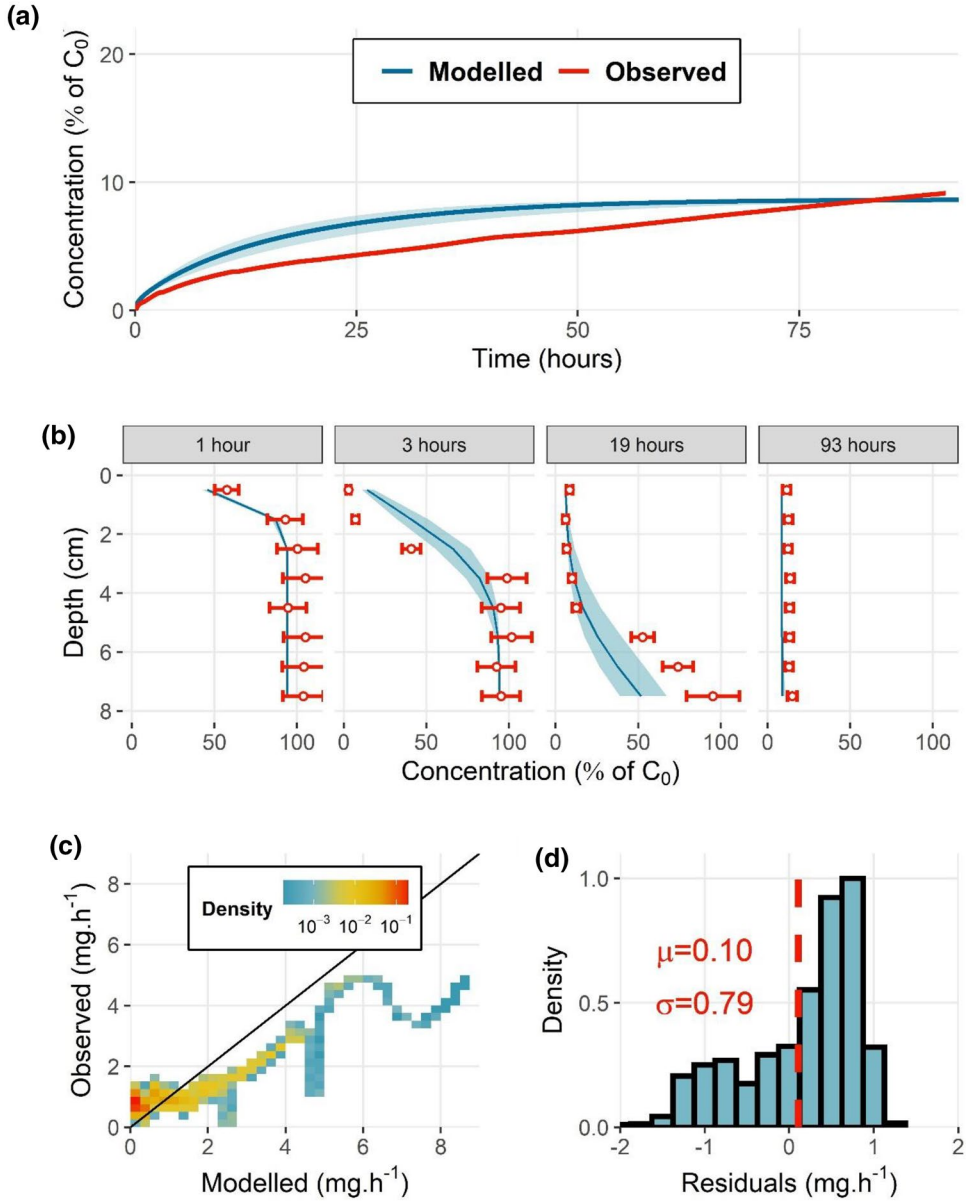

Figure 3. Experimental and modeled results of the EHF_{NaCl} experiment. (a) Evolution of normalized tracer concentrations by the initial tracer concentration in the mixing beaker (C/C_0). Analytical uncertainties of NaCl concentration measurements are smaller than the line thickness. (b) Observed and modeled tracer vertical distribution in the sediment bed. In A and B, the blue shaded areas correspond to the numerical confidence interval including experimental uncertainties of K_0 and u^*. (c) Modeled (Φ_M) and observed (Φ_O) mass fluxes at the sediment-water interface (reported in mg·h^{-1} of tracer and calculated at each time step from the evolution of concentrations within the mixing beaker), and (d) residuals of the difference $\Phi_O - \Phi_M$ (μ and σ stand for the mean and the standard deviation of residual distribution).

Some offsets reflected transient experimental conditions. Equilibrium was reached within the sediment bed after 93 h in the EHF_{NaCl} experiment. However, at the end of the experiments with NaCl, the slight and steady increases of NaCl concentrations in the mixing beaker could be attributed to the unintended release of ions from the sand, although it was thoroughly washed. In contrast, the spectrophotometric measurements of FB291 were not affected by experimental bias. For further tests, fluorescent conservative tracers (e.g., fluorescein sodium salt—CAS Number: 518-47-8), measurable using spectrophotometric methods, may be a valuable alternative to NaCl. The experimental results were also highly sensitive to minor water

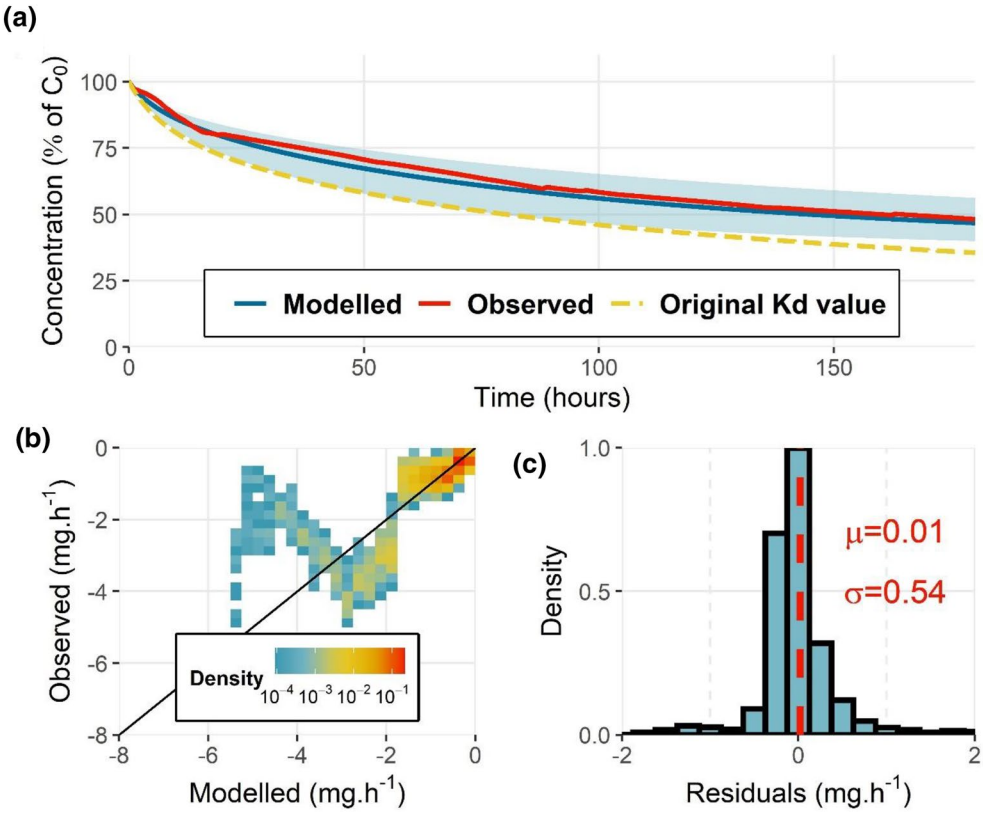

Figure 4. Experimental and modeled results for IHF_{FB291}. (a) Evolution of normalized tracer concentration dynamic in the mixing beaker. Analytical uncertainties of FB291 concentration measurements are smaller than the line thickness; (b) Modeled (Φ_M) and observed (Φ_O) mass fluxes at the sediment-water interface, and (c) residuals of the difference $\Phi_O - \Phi_M$.

height instabilities (±2 mm) under high flow, which resulted in variations of the overlying water velocities. An automatic limitation of water height in the channel may be useful for future experiments. Although these experimental limitations punctually affected observations, they did not question the validity of the procedure as the overall tendencies were well reproduced.

5. Results of the Bench-Scale River Channel

5.1. The Velocity Field

Understanding the velocity field is fundamental for interpreting pollutant transport and exchange fluxes at the SWI, although experimental visualization of the velocity field is tedious. Numerical simulations can help to follow-up velocity variation across the domain and identify dominant transport processes in the bench-scale river channel.

Streamlines are plotted in Figure 5a. Distinct velocity patterns in the sediment bed occurred across the domain (Figure 5b). In the overlying water, the model reproduced the log-law of wall profile with a nonnull slip velocity at the interface (Nagaoka & Ohgaki, 1990; Rosti et al., 2015) (Text S6). Despite the small size of the experimental setup, the effect of surface tension on the sidewalls of the channel was considered negligible. The velocity profile prediction by the Navier-Stokes equation was assumed appropriate, although velocity was not directly measured (Malverti et al., 2008). The simulated velocities in the transition layer abruptly dropped by several orders of magnitude and reached a value close to the Darcy velocity (v_{Darcy}) (Text S7 for calculation details).

The simulated velocity in the sediment bed over the transition layer shows similar profile as in the previous observations in Goharzadeh et al. (2005), i.e. logarithmic vertical velocity distribution. Hence, the model

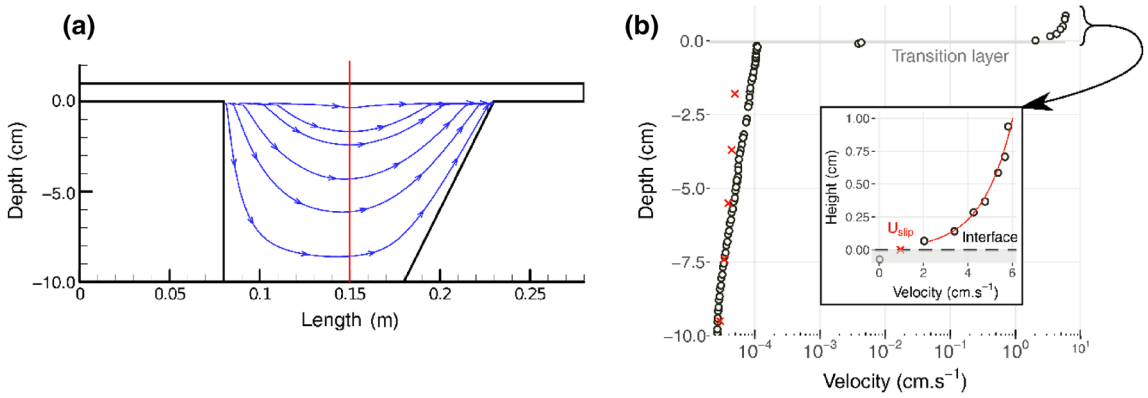

Figure 5. (a) Streamlines in the domain showing the pumping effect that may be caused by bedforms in rivers. The vertical red line represents the axis where velocities were extracted in panel B. (b) Modeled velocity profile (circles) and Darcy's velocities (red crosses). The gray shaded area represents the transition layer defined in the numerical domain. The black box zooms in on the overlying water velocity profile and fitting results with the log-law of wall (solid red line).

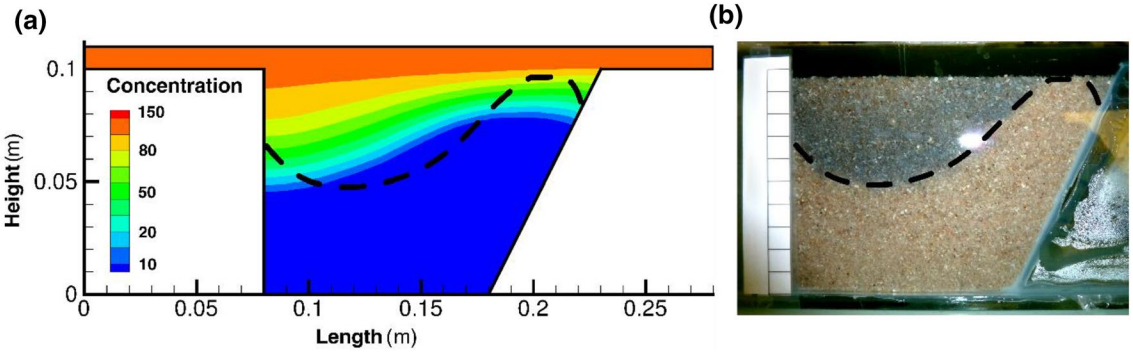

Figure 6. (a) Numerical and (b) experimental distribution of FB291 within the sediment bed after 12 h under IHF_{FB291} conditions. The black dashed line in panel B corresponds to the limit of FB291 penetration observed and is reported in panel A for direct comparison with numerical results.

could reliably predict the velocity profiles in the sediment bed, without imposing any interface conditions (Bars & Worster, 2006). This observation is of great importance since the velocity profile in the sediment controls the pollutant exchange at the SWI (Nagaoka & Ohgaki, 1990; Voermans et al., 2017). Below the transition layer, the pressure gradient at the interface mainly controlled the water flow. This control indicates a minor effect of viscosity in the sediment bed. Considering the size of the experimental setup (15 cm long and 10 cm deep) and the control of flow within the sediment bed by pressure distribution alongside the interface, the system accurately reproduced the pumping flow caused by bed-forms in actual rivers (Cardenas & Wilson, 2007a; Kaufman et al., 2017). This underscores that the experimental setup and the developed model are suited to predict mass exchange driven by hydrodynamic (e.g., bed forms, rapid variations of water flow, inhomogeneity of sediment permeability, etc.) and hydrostatic (e.g., riverbed topography, meanders, etc.) forces, characterizing small- and large scale-rivers, respectively.

5.2. Transport Processes and Mass Exchange

Similar patterns of NaCl concentrations were observed in the sediment bed and the mixing beaker, regardless of the configurations (i.e., $ILF_{NaCl} \sim ELF_{NaCl}$ and $IHF_{NaCl} \sim EHF_{NaCl}$). Under similar flow conditions, the simulated times to reach 80% of equilibrium concentrations between export and incorporation cases were similar (Table 1). Since the export and incorporation cases are the exact opposite experiments, a riverbed sediment would incorporate or release pollutants at equivalent rates. The proposed approach could then be applied in the future to investigate the transport of pollutants stemming either from the overlying water

(e.g., diffuse or punctual contaminations) or from the riverbed sediment (e.g., groundwater or anterior contamination of the sediment bed), when pollutant sorption is insignificant.

The upper part of the sediment bed was rapidly and strongly affected by a concentration gradient imposed by the overlying water (Figure 3b). Pollutant transport in the sediment bed decreases with increasing depth, as already reported in Chandler et al. (2016). Hence, the deeper the pollutant location in the sediment bed is, the less interaction with the overlying water.

The results also emphasize that mass exchange at the SWI is sensitive to the overlying water velocity. Indeed, a higher water flow increases Darcy's velocity and penetration of the overlying water velocities into the sediment bed (Habel et al., 2002). It is also worth noting that the velocity ratios between low and high flows corresponded to those of the simulated characteristic times ($t_{80\%}$), which were about three-fold longer under low flow than high flow (Table 1). Accordingly, the nature of the dominant transport process (i.e., diffusion, dispersion, or advection) governing the overall mass exchange may remain equivalent within the range of tested velocities (i.e., 1.4–4.7 cm·s^{-1} for NaCl). In addition, the contribution of diffusion to the overall transport may be modest: the rate of mass exchange with time may be unaffected by velocity changes as the magnitude of diffusion only depends on concentration gradients.

The nature of the dominant transport process can also be inferred from calculation of the Peclet number (Pe) over the depth as it expresses the ratio of advection over diffusion or dispersion (Chandler et al., 2016; Pinay et al., 2015). Detailed calculation procedures for Pe and D_{eff} are provided in Text S8 and Text S9. The calculation of effective diffusivities (D_{eff}), as used in the diffusive models, also helps to characterize the overall dominant transport process. Indeed, the value of D_{eff} reflects the dominant transport process driving mass exchange at the SWI, being either diffusion ($\frac{D_{eff}}{D_m} \approx 1$) or dispersion and turbulent advection ($\frac{D_{eff}}{D_m} > 1$) (Grant et al., 2012; Voermans et al., 2018).

In our case, Pe from 5 to 100 (except at the very bottom of the sediment bed under low flow condition) confirmed the limited effect of diffusion over advection. In addition, calculation of the effective diffusivities for low and high flow conditions revealed that diffusion was outranked by a factor of $\frac{D_{eff}}{D_m} = 3.8$ and $\frac{D_{eff}}{D_m} = 15.2$ by diffusion in low and high flow, respectively. According to Voermans et al. (2017), these ratios indicate dispersion-dominated transport regimes. Finally, water flow and $t_{80\%}$ could not be related with the equivalent riverbed travel length ($L_{eq,80\%}(t) = u^* \cdot t_{80\%}$), which does not change under low and high flow conditions when the dominant transport process is the same (see Table 1). The total mass of tracer exchanged per length unit of riverbed was thus independent from the overlying water velocities under these conditions. In the absence of degradation and/or sorption, the flow-independent exchange capacity of a river transect can be inferred from the physical characteristics of the riverbed (geometry and permeability).

5.3. Effect of Sorption on Mass Exchange at the SWI

Pollutant sorption can significantly increase the experimental duration. Equilibrium was not reached in the experiment with FB291 (Figure 4a), even after 7 and 4 times longer duration (for EHF_{FB291} and IHF_{FB291}, respectively) than in the experiments with NaCl under similar flow conditions. In the case of incorporation, this duration was attributed to sorption at the front edge of the tracer plume, which retarded its progression (Schaffer & Licha, 2015). In the case of export, the slower desorption kinetics of FB291 likely delayed its release from the sediment bed (Ren & Packman, 2004b). Partitioning between the aqueous phase and the sediment grain surfaces also decreased FB291 concentrations in the liquid phase. Although equilibria were not fully established, it is estimated that up to 58% (EHF_{FB291}) and 42% (IHF_{FB291}) of the initial FB291 mass were sorbed to the sediment at the end of the experiments with FB291. Overall, the sorption increased the amount of tracer incorporated into the sediment bed compared with NaCl, which limited the FB291 mobility in the overlying water.

Most importantly, the model predicted less FB291 sorption to the sediment under dynamic conditions than that observed in the batch characterization. In the export case, equilibrium was not reached but the FB291

concentrations emphasized that the amount of tracer released to the water column was larger than that derived from the C_{eq} value using $K_d = 7.7$ mL·g^{-1}. In addition, predictions using the experimental K_d value excessively retarded the plume penetration compared to the observed penetration (data not shown). As exemplified by the dashed yellow line in Figure 4a, the use of the experimental K_d value led to an overestimation of the decrease of FB291 concentrations in the overlying water during IHF_{FB291}. In contrast, during EHF_{FB291} the experimental K_d value led to a weaker FB291 release into the overlying water than that actually observed. Finally, accurate reproduction of export and incorporation configurations with the same calibrated K_d value suggests that sorption isotherm for FB291 from quartz sand is reversible, as previously observed for metal ions (Eylers et al., 1995; Ren & Packman, 2004a). Altogether, this isotherm validates the mathematical implementation of sorption in the FRT model.

The discrepancy between the calibrated and experimentally derived K_d values can be explained by the validity of the linear isotherm implemented in the model, although the laboratory characterization was unambiguous (see Text S2). In addition, the adsorption kinetic may have affected the progression of the tracer plume (Eylers et al., 1995). While the pseudo-first-order kinetic implemented in the model is well suited for FB291 sorption, the rate of 12 h ($\alpha = 8.3{\cdot}10^{-5}$s^{-1}), chosen as a maximal value ensuring complete equilibrium, can be argued because FB291 sorption on clay materials has been reported to take place in a few hours (Berez et al., 2016). However, the interactions with clay material are potentially stronger than that with sand surfaces, favoring rapid sorption (Berez et al., 2014). In addition, a quicker sorption rate may further exacerbate the depletion of FB291 concentration in the mixing beaker and further delay FB291 penetration, which is inconsistent with our observations (Figure 6b). Finally, the constant shaking in the batch sorption equilibrium method largely differs from mixing occurring in packed sediment beds, which naturally limits pollutant exposure to sediment grain surfaces. This statement agrees with previous observations of enhanced sorption in stirred systems where sediment grinding resulted in more available sorption sites than in shaken systems (Shrestha et al., 2016).

Altogether, the sorption increased pollutant incorporation, hampered export, and decreased pollutant concentrations in pore water compared to conservative tracers. Accordingly, the sink role of riverbed sediments is exacerbated for sorptive pollutants (Ren & Packman, 2004a). Meanwhile, the sorption increases pollutant residence time within the riverbed by retarding its release to the overlying water (Eylers et al., 1995). Sorption also limits pollutant penetration toward the deepest sediment layers (Liao et al., 2013).

6. Toward a Comprehensive Understanding of Hyporheic Processes at the SWI

The experimental setup generally focused on the effect of overlying water dynamics to interpret mass exchange at the SWI and circumvent the relationship between the river and groundwater. However, at the river scale, surface-ground water interactions also control hyporheic mass exchange as well as the nature and magnitude of biogeochemical processes (Byrne et al., 2014). The effect of vertical hydraulic fluxes (i.e., upwelling or downwelling) on mass exchange at the SWI thus has to be considered when upscaling to the reach scale (Lansdown et al., 2015). While most of the diffusive and multidomain models do not address vertical fluxes as detailed in the introduction, our model allows for investigating the combined effect of overlying water velocity and vertical hydraulic gradient on mass exchange at the SWI.

To illustrate this combined effect, we examined a numerical test over a 1 m long (L) river reach with polluted overlying water ($C = 1$ mg·L^{-1}) connected from below with a pristine groundwater ($C = 0$ mg·L^{-1}). We considered 50 cm of sediment ($K_0 = 7.4 \pm 2.2{\cdot}10^{-4}$ m·s^{-1}, as for the sand used in the river channel) and 10 cm of overlying water (as depicted in Figure 7) which is in accordance with the actual scale of hyporheic processes (Boano et al., 2014). The range of vertical fluxes tested was chosen to represent low Strahler order rivers ($v_{gw} \in \left[-0.10;0.30\right]$ in m·d^{-1}) (Binley et al., 2013). The overlying water velocities were chosen to satisfy the laminar flow assumption ($Re \in \{500, 1{,}000, 4{,}000\}$, or $v_w \in \left\{0.05, 0.01, 0.04\ \text{cm·s}^{-1}\right\}$) (Sparrow et al., 1973). The effect of sorption was also tested to identify the typical behavior of moderately to strongly hydrophobic pollutants ($K_d \in \left\{0, 2, 7\right\}$ mL·g^{-1}). The total pollutant mass flux (Φ) was calculated alongside the 1 m long interface as the sum of advective (Φ_{adv}) and dispersive (Φ_{disp}) fluxes.

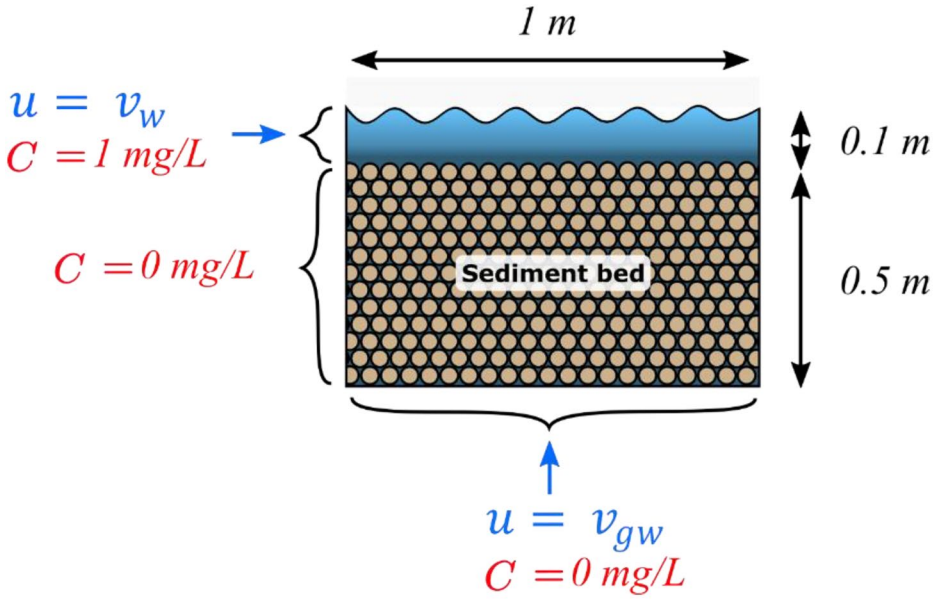

Figure 7. Numerical domain representing a 1 m long typical river reach. Wherever boundary conditions are not reported, opened boundary were set.

In the absence of vertical velocities (i.e., $v_{gw} = 0$ m·d^{-1}), regardless of the horizontal water flow, mass fluxes through the interface was driven by diffusion ($10^{-2} < \frac{\Phi_{adv}}{\Phi_{disp}} < 10^{-1}$). The absence of pressure gradients across the SWI (e.g., bedforms, instream obstacles, etc.) limited the infiltration of the overlying water in the sediment bed, which limited advection-driven transport. Thus, the vertical velocity strongly controls the mass fluxes through the SWI (see Figure 8a). As a rule of thumb, the decrease of pollutant penetration within the SWI observed for dimensionless upwelling velocities was one order of magnitude higher than the predicted dimensionless mass flux for $v_{gw} = 0$ m·d^{-1}($\hat{\Phi}_0$). In contrast, for dimensionless downwelling velocities higher than about $\hat{\Phi}_0$, the mass fluxes became exclusively driven by advection. In the latter case, pollutant mass flux through the interface can be estimated as the product $\Phi = C_w \cdot v_{gw}$. This prediction is in line with previous observations demonstrating the existence of a threshold of $|v_{gw}|$ above which vertical fluxes are the dominant mechanism of water exchanges at the interface (Fox et al., 2014).

The effect of sorption on pollutant penetration was remarkable even with K_d as low as 2 mL·g^{-1} (Figure 8b). For instance, after 16 days of simulation with a downwelling flux $v_{gw} = 0.01$ m·d^{-1}, while the nonsorptive pollutant reached the bottom of the numerical domain, sorptive pollutants with $K_d = 2.0$ and 7.0 mL·g^{-1} only penetrated the top 20 and 10 cm of sediment (see Figure 8b). Accordingly, the propensity of a pollutant to sorb onto the sediment bed is an important feature to account for in actual river systems as it may significantly reduce the river contribution to groundwater pollution. It also highlights the fact that in riverbed, pollutant likely accumulates within the first centimeters of the sediment.

Altogether, these observations confirm (1) the ability of the model to handle surface-ground water interactions at the river scale (i.e., computation time ≈10 min for a 16 daylong simulated period), (2) the major control of vertical velocity on pollutant mass exchange at the SWI, and (3) the crucial role of sorption on pollutant penetration pace within the sediment bed.

7. Conclusions

The variability of pollutant fluxes at the SWI is multifactorial and often overlooked at large scales. Experimental and numerical developments are thus required to improve the interpretation of pollutant behavior at the river scale. This work showcases an experimental and model development for generic evaluation of pollutant transport at the SWI.

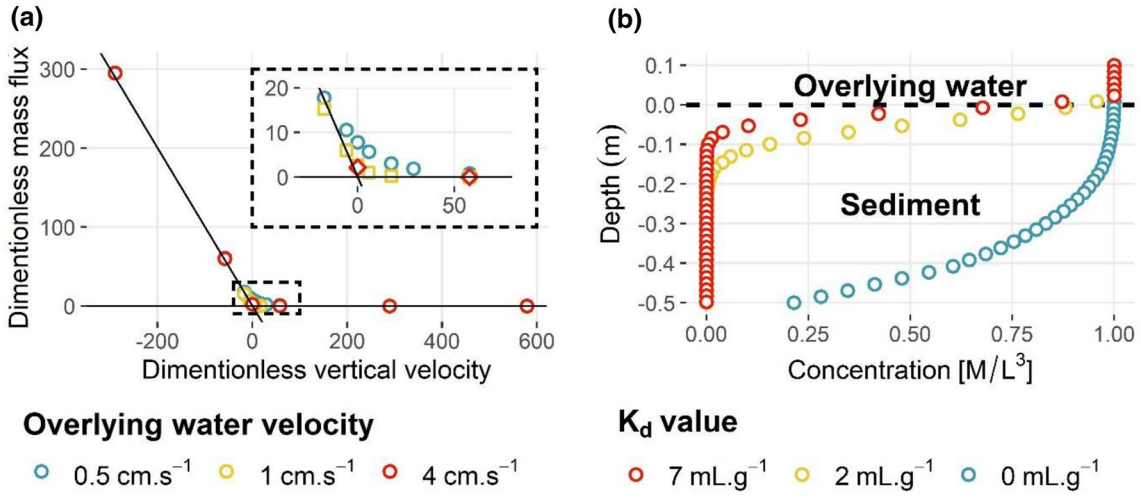

Figure 8. (a) Modeled dimensionless mass flux ($\hat{\Phi} = \frac{\Phi}{L \cdot D_m \cdot C}$; y-axis) crossing the SWI under various upwelling (negative velocity) and downwelling (positive velocity) conditions ($\hat{v}_{gw} = \frac{v_{gw} \cdot L}{D_m}$; x-axis) and overlying water velocity (colors and legend). (b) Modeled pollutant penetration within the sediment bed with $v_{gw} = 0.01$ m·d^{-1} and $v_w = 0.04$ m·s^{-1} and varying sorption strengths from sorptive (red) to nonsorptive (blue) pollutant (K_d in mL·g^{-1}).

The experimental setup allowed for reproducing the transport of conservative and sorptive pollutants over riverbeds with bedforms. Relying on advanced numerical techniques, the developed model improved the interpretation of pollutant transport in a bench-scale experimental river channel. The experimental results fitted those of numerical simulations with a restrained calibration procedure. The pollutant mass exchange at the SWI positively correlated with the water flow regardless of whether the pollutant originates from the overlying water or the sediment bed. The sorption of FB291 tracer retarded pollutant export downstream and strengthened the role of sink played by the sediment bed. The coupled procedure also emphasized that classical batch sorption experiments may not be suited to predict sorption to riverbed sediment under dynamic conditions. To advance in an applicable methodology to investigate pollutant behaviour in river systems, we coupled the SWI with upwelling/downwelling velocities over a 1 m long river reach. It highlighted the crucial role of bedforms and vertical velocities in driving mass exchange at the SWI. It also revealed that sorption largely limited pollutant penetration into the sediment bed.

Overall, these results may help in the future to improve interpretation of pollutant fate in river systems accounting for complex water fluxes originating from their surrounding environment (e.g., surface-groundwater fluxes). Further developments with this code are nonetheless needed to resolve pollutant transport in large rivers featuring turbulent flow. While the laminar flow assumption holds for rivers with small currents, artificial ponds, or lakes, vertical velocities generated by eddies may enhance pollutant penetration within the SWI, even over flatbeds in rivers undergoing turbulent flow. The implementation of a turbulent closure scheme to the momentum equation would help to represent a large panel of environmentally relevant river conditions. We anticipate that future research, building on these experimental and numerical developments may include transient storage during flood events, the effect of varying sediment bed geometries, or large-scale features such as dams or meanders on pollutant exchange rates, or the relationship between organic matter cycling and sediment diagenesis and pollutant degradation.

Data Availability Statement

Experimental and numerical data as well as the developed numerical are available on Mendeley Data, V1, https://doi.org/10.17632/myyghj4nnh.1

Acknowledgments
G. Drouin was supported by the French Ministry for the Ecological Transition. B. Droz was supported by the Region Grand Est and the Rhine-Meuse Water Agency. This study was funded by the Rhine-Meuse Water Agency (Project PolISO n°170293) and the French National research Agency ANR through grant ANR-18-CE32-0007, project PESTIPOND. The authors would like to acknowledge 2 anonymous reviewers for their helpful comments and suggestions, as well as Margaret Johnson and Solenn Cotel for their help with experimental design and analytical measurements.

References

Allen, J. (1965). Laminar and Turbulent Flow in Open Channels. *Nature*, *208*(5016), 1196–1197. https://doi.org/10.1038/2081196a0

Angot, P., Goyeau, B., & Ochoa-Tapia, J. A. (2017). Asymptotic modeling of transport phenomena at the interface between a fluid and a porous layer: Jump conditions. *Physical Review E*, *95*(6), 063302. https://doi.org/10.1103/PhysRevE.95.063302

Bars, M. L., & Worster, M. G. (2006). Interfacial conditions between a pure fluid and a porous medium: Implications for binary alloy solidification. *Journal of Fluid Mechanics*, *550*, 149–173. https://doi.org/10.1017/S0022112005007998

Battiato, I., & Rubol, S. (2014). Single-parameter model of vegetated aquatic flows. *Water Resources Research*, *50*(8), 6358–6369. https://doi.org/10.1002/2013WR015065

Berez, A., Ayari, F., Abidi, N., Schäfer, G., Trabelsi-Ayadi, M., & Ferrage, E. (2014). Adsorption-desorption processes of azo dye on natural bentonite: Batch experiments and modelling. *Clay Minerals*, *49*(5), 747–763. https://doi.org/10.1180/claymin.2014.049.5.10

Berez, A., Schäfer, G., Ayari, F., & Trabelsi-Ayadi, M. (2016). Adsorptive removal of azo dyes from aqueous solutions by natural bentonite under static and dynamic flow conditions. *International Journal of Environmental Science and Technology*, *13*(7), 1625–1640. https://doi.org/10.1007/s13762-016-1006-3

Binley, A., Ullah, S., Heathwaite, A. L., Heppell, C., Byrne, P., Lansdown, K., et al. (2013). Revealing the spatial variability of water fluxes at the groundwater-surface water interface. *Water Resources Research*, *49*(7), 3978–3992. https://doi.org/10.1002/wrcr.20214

Boano, F., Harvey, J. W., Marion, A., Packman, A. I., Revelli, R., Ridolfi, L., & Wörman, A. (2014). Hyporheic flow and transport processes: Mechanisms, models, and biogeochemical implications. *Reviews of Geophysics*, *52*(4), 603–679. https://doi.org/10.1002/2012RG000417

Briggs, M. A., Lautz, L. K., & Hare, D. K. (2014). Residence time control on hot moments of net nitrate production and uptake in the hyporheic zone. *Hydrological Processes*, *28*(11), 3741–3751. https://doi.org/10.1002/hyp.9921

Burman, E., & Hansbo, P. (2005). Stabilized Crouzeix-Raviart element for the Darcy-Stokes problem. *Numerical Methods for Partial Differential Equations*, *21*(5), 986–997. https://doi.org/10.1002/num.20076

Byrne, P., Binley, A., Heathwaite, A. L., Ullah, S., Heppell, C. M., Lansdown, K., et al. (2014). Control of river stage on the reactive chemistry of the hyporheic zone. *Hydrological Processes*, *28*(17), 4766–4779. https://doi.org/10.1002/hyp.9981

Cardenas, M. B., & Wilson, J. L. (2007a). Dunes, turbulent eddies, and interfacial exchange with permeable sediments. *Water Resources Research*, *43*(8). https://doi.org/10.1029/2006WR005787

Cardenas, M. B., & Wilson, J. L. (2007b). Hydrodynamics of coupled flow above and below a sediment–water interface with triangular bedforms. *Advances in Water Resources*, *30*(3), 301–313. https://doi.org/10.1016/j.advwatres.2006.06.009

Carman, P. C. (1997). Fluid flow through granular beds. *Chemical Engineering Research and Design*, *75*, S32–S48. https://doi.org/10.1016/S0263-8762(97)80003-2

Chandler, I. D., Guymer, I., Pearson, J. M., & van Egmond, R. (2016). Vertical variation of mixing within porous sediment beds below turbulent flows. *Water Resources Research*, *52*(5), 3493–3509. https://doi.org/10.1002/2015WR018274

Downing, J. (2012). Global abundance and size distribution of streams and rivers. *Inland Waters*, *2*(4), 229–236. https://doi.org/10.5268/IW-2.4.502

Dwivedi, D., Steefel, C. I., Arora, B., Newcomer, M., Moulton, J. D., Dafflon, B., et al. (2018). Geochemical Exports to River From the Intrameander Hyporheic Zone Under Transient Hydrologic Conditions: East River Mountainous Watershed, Colorado. *Water Resources Research*, *54*(10), 8456–8477. https://doi.org/10.1029/2018WR023377

Ehrhardt, M. (2012). Progress in Computational Physics (PiCP). Coupled Fluid Flow in Energy, Biology and Environmental Research (Vol. 2). Sharjah UAE: Bentham Science Publishers.

Eylers, H., Brooks, N. H., & Morgan, J. J. (1995). Transport of adsorbing metals from stream water to a stationary sand-bed in a laboratory flume. *Marine and Freshwater Research*, *46*(1), 209–214. https://doi.org/10.1071/mf9950209

Fahs, M., Carrayrou, J., Younes, A., & Ackerer, P. (2008). On the Efficiency of the Direct Substitution Approach for Reactive Transport Problems in Porous Media. *Water, Air, and Soil Pollution*, *193*(1), 299–308. https://doi.org/10.1007/s11270-008-9691-2

Fahs, M., & Younes, A. (2014). A High-Accurate Fourier-Galerkin Solution for Buoyancy-Driven Flow in a Square Cavity. *Numerical Heat Transfer, Part B: Fundamentals*, *65*(6), 495–517. https://doi.org/10.1080/10407790.2014.884832

Fahs, M., Younes, A., & Ackerer, P. (2011). An Efficient Implementation of the Method of Lines for Multicomponent Reactive Transport Equations. *Water, Air, & Soil Pollution*, *215*(1), 273–283. https://doi.org/10.1007/s11270-010-0477-y

Fernandez-Pascual, E., Bork, M., Hensen, B., & Lange, J. (2020). Hydrological tracers for assessing transport and dissipation processes of pesticides in a model constructed wetland system. *Hydrology and Earth System Sciences*, *24*(1), 41–60. https://doi.org/10.5194/hess-24-41-2020

Fox, A., Boano, F., & Arnon, S. (2014). Impact of losing and gaining streamflow conditions on hyporheic exchange fluxes induced by dune-shaped bed forms. *Water Resources Research*, *50*(3), 1895–1907. https://doi.org/10.1002/2013WR014668

Franca, M. J., Ferreira, R. M. L., & Lemmin, U. (2008). Parameterization of the logarithmic layer of double-averaged streamwise velocity profiles in gravel-bed river flows. *Advances in Water Resources*, *31*(6), 915–925. https://doi.org/10.1016/j.advwatres.2008.03.001

Goharzadeh, A., Khalili, A., & Jørgensen, B. B. (2005). Transition layer thickness at a fluid-porous interface. *Physics of Fluids*, *17*(5), 057102. https://doi.org/10.1063/1.1894796

Grant, S. B., & Marusic, I. (2011). Crossing turbulent boundaries: Interfacial flux in environmental flows. *Environmental Science & Technology*, *45*(17), 7107–7113. https://doi.org/10.1021/es201778s

Grant, S. B., Stewardson, M. J., & Marusic, I. (2012). Effective diffusivity and mass flux across the sediment-water interface in streams. *Water Resources Research*, *48*(5). https://doi.org/10.1029/2011WR011148

Habel, F., Mendoza, C., & Bagtzoglou, A. C. (2002). Solute transport in open channel flows and porous streambeds. *Advances in Water Resources*, *25*(4), 455–469. https://doi.org/10.1016/S0309-1708(01)00052-5

Harned, H. S., & Hildreth, C. L. (1951). The Differential Diffusion Coefficients of Lithium and Sodium Chlorides in Dilute Aqueous Solution at 25°. *Journal of the American Chemical Society*, *73*(2), 650–652. https://doi.org/10.1021/ja01146a043

Hirthe, E. M., & Graf, T. (2012). Non-iterative adaptive time-stepping scheme with temporal truncation error control for simulating variable-density flow. *Advances in Water Resources*, *49*, 46–55. https://doi.org/10.1016/j.advwatres.2012.07.021

Honti, M., Bischoff, F., Moser, A., Stamm, C., Baranya, S., & Fenner, K. (2018). Relating Degradation of Pharmaceutical Active Ingredients in a Stream Network to Degradation in Water-Sediment Simulation Tests. *Water Resources Research*, *54*(11), 9207–9223. https://doi.org/10.1029/2018WR023592

Jada, A., & Ait Akbour, R. (2014). Adsorption and Removal of Organic Dye at Quartz Sand-Water Interface. *Oil & Gas Science and Technology – Revue d'IFP Energies Nouvelles*, *69*(3), 405–413. https://doi.org/10.2516/ogst/2013169

Jin, G., Chen, Y., Tang, H., Zhang, P., Li, L., & Barry, D. A. (2019). Interplay of hyporheic exchange and fine particle deposition in a riverbed. *Advances in Water Resources*, *128*, 145–157. https://doi.org/10.1016/j.advwatres.2019.04.014

Kaufman, M. H., Cardenas, M. B., Buttles, J., Kessler, A. J., & Cook, P. L. M. (2017). Hyporheic hot moments: Dissolved oxygen dynamics in the hyporheic zone in response to surface flow perturbations: Dissolved oxygen dynamics in the hyporheic zone. *Water Resources Research*, *53*(8), 6642–6662. https://doi.org/10.1002/2016WR020296

Kiecak, A., Breuer, F., & Stumpp, C. (2019). Column Experiments on Sorption Coefficients and Biodegradation Rates of Selected Pharmaceuticals in Three Aquifer Sediments. *Water*, *12*(1), 14. https://doi.org/10.3390/w12010014

Krause, S., Lewandowski, J., Grimm, N. B., Hannah, D. M., Pinay, G., McDonald, K., et al. (2017). Ecohydrological interfaces as hot spots of ecosystem processes. *Water Resources Research*, *53*(8), 6359–6376. https://doi.org/10.1002/2016WR019516

Lācis, U., & Bagheri, S. (2017). A framework for computing effective boundary conditions at the interface between free fluid and a porous medium. *Journal of Fluid Mechanics*, *812*, 866–889. https://doi.org/10.1017/jfm.2016.838

Lansdown, K., Heppell, C. M., Trimmer, M., Binley, A., Heathwaite, A. L., Byrne, P., & Zhang, H. (2015). The interplay between transport and reaction rates as controls on nitrate attenuation in permeable, streambed sediments. *Journal of Geophysical Research: Biogeosciences*, *120*(6), 1093–1109. https://doi.org/10.1002/2014JG002874

Lewandowski, J., Arnon, S., Banks, E., Batelaan, O., Betterle, A., Broecker, T., et al. (2019). Is the Hyporheic Zone Relevant beyond the Scientific Community? *Water*, *11*(11), 2230. https://doi.org/10.3390/w11112230

Liao, Z., Lemke, D., Osenbrück, K., & Cirpka, O. A. (2013). Modeling and inverting reactive stream tracers undergoing two-site sorption and decay in the hyporheic zone. *Water Resources Research*, *49*(6), 3406–3422. https://doi.org/10.1002/wrcr.20276

Liu, Y., Wallace, C. D., Zhou, Y., Ershadnia, R., Behzadi, F., Dwivedi, D., et al. (2020). Influence of Streambed Heterogeneity on Hyporheic Flow and Sorptive Solute Transport. *Water*, *12*(6), 1547. https://doi.org/10.3390/w12061547

Malverti, L., Lajeunesse, E., & Métivier, F. (2008). Small is beautiful: Upscaling from microscale laminar to natural turbulent rivers. *Journal of Geophysical Research: Earth Surface*, *113*(F4). https://doi.org/10.1029/2007JF000974

Miller, C. T., Dawson, C. N., Farthing, M. W., Hou, T. Y., Huang, J., Kees, C. E., et al. (2013). Numerical simulation of water resources problems: Models, methods, and trends. *Advances in Water Resources*, *51*, 405–437. https://doi.org/10.1016/j.advwatres.2012.05.008

Munz, M., Krause, S., Tecklenburg, C., & Binley, A. (2011). Reducing monitoring gaps at the aquifer–river interface by modelling groundwater–surface water exchange flow patterns. *Hydrological Processes*, *25*(23), 3547–3562. https://doi.org/10.1002/hyp.8080

Nagaoka, H., & Ohgaki, S. (1990). Mass transfer mechanism in a porous riverbed. *Water Research*, *24*(4), 417–425. https://doi.org/10.1016/0043-1354(90)90223-S

Nield, D. A. (1983). The boundary correction for the Rayleigh-Darcy problem: Limitations of the Brinkman equation. *Journal of Fluid Mechanics*, *128*, 37–46. https://doi.org/10.1017/S0022112083000361

OECD (2000). *Test No. 106: Adsorption -- Desorption Using a Batch Equilibrium Method*. Paris: Organisation for Economic Co-operation and Development. Retrieved from http://www.oecd-ilibrary.org/content/book/9789264069602-en

Pinay, G., Peiffer, S., De Dreuzy, J.-R., Krause, S., Hannah, D. M., Fleckenstein, J. H., et al. (2015). Upscaling Nitrogen Removal Capacity from Local Hotspots to Low Stream Orders' Drainage Basins. *Ecosystems*, *18*(6), 1101–1120. https://doi.org/10.1007/s10021-015-9878-5

Ren, J., & Packman, A. I. (2004a). Modeling of Simultaneous Exchange of Colloids and Sorbing Contaminants between Streams and Streambeds. *Environmental Science & Technology*, *38*(10), 2901–2911. https://doi.org/10.1021/es034852l

Ren, J., & Packman, A. I. (2004b). Stream-Subsurface Exchange of Zinc in the Presence of Silica and Kaolinite Colloids. *Environmental Science & Technology*, *38*(24), 6571–6581. https://doi.org/10.1021/es035090x

Rosti, M. E., Cortelezzi, L., & Quadrio, M. (2015). Direct numerical simulation of turbulent channel flow over porous walls. *Journal of Fluid Mechanics*, *784*, 396–442. https://doi.org/10.1017/jfm.2015.566

Salim Joodi, A., Sizaret, S., Binet, S., Bruand, A., Albéric, P., & Lepiller, M. (2010). Development of a Darcy-Brinkman model to simulate water flow and tracer transport in a heterogeneous karstic aquifer (Val d'Orléans, France). *Hydrogeology Journal*, *18*(2), 295–309. https://doi.org/10.1007/s10040-009-0536-x

Schaffer, M., & Licha, T. (2015). A framework for assessing the retardation of organic molecules in groundwater: Implications of the species distribution for the sorption-influenced transport. *Science of The Total Environment*, *524*(525), 187–194. https://doi.org/10.1016/j.scitotenv.2015.04.006

Shrestha, P., Junker, T., Fenner, K., Hahn, S., Honti, M., Bakkour, R., et al. (2016). Simulation Studies to Explore Biodegradation in Water–Sediment Systems: From OECD 308 to OECD 309. *Environmental Science & Technology*, *50*(13), 6856–6864. https://doi.org/10.1021/acs.est.6b01095

Sousa, J. C. G., Ribeiro, A. R., Barbosa, M. O., Pereira, M. F. R., & Silva, A. M. T. (2018). A review on environmental monitoring of water organic pollutants identified by EU guidelines. *Journal of Hazardous Materials*, *344*, 146–162. https://doi.org/10.1016/j.jhazmat.2017.09.058

Sparrow, E. M., Beavers, G. S., Chen, T. S., & Lloyd, J. R. (1973). Breakdown of the Laminar Flow Regime in Permeable-Walled Ducts. *Journal of Applied Mechanics*, *40*(2), 337–342. https://doi.org/10.1115/1.3422984

Suga, K., Matsumura, Y., Ashitaka, Y., Tominaga, S., & Kaneda, M. (2010). Effects of wall permeability on turbulence. *International Journal of Heat and Fluid Flow*, *31*(6), 974–984. https://doi.org/10.1016/j.ijheatfluidflow.2010.02.023

Tian, Z., & Wang, J. (2017). Lattice Boltzmann simulation of CO_2 reactive transport in network fractured media. *Water Resources Research*, *53*(8), 7366–7381. https://doi.org/10.1002/2017WR021063

Tian, Z., & Wang, J. (2018). Lattice Boltzmann simulation of dissolution-induced changes in permeability and porosity in 3D CO_2 reactive transport. *Journal of Hydrology*, *557*, 276–290. https://doi.org/10.1016/j.jhydrol.2017.12.037

Valdés-Parada, F. J., Aguilar-Madera, C. G., Ochoa-Tapia, J. A., & Goyeau, B. (2013). Velocity and stress jump conditions between a porous medium and a fluid. *Advances in Water Resources*, *62*, 327–339. https://doi.org/10.1016/j.advwatres.2013.08.008

van Genuchten, M. Th., & Wagenet, R. J. (1989). Two-Site/Two-Region Models for Pesticide Transport and Degradation: Theoretical Development and Analytical Solutions. *Soil Science Society of America Journal*, *53*(5), 1303. https://doi.org/10.2136/sssaj1989.03615995005300050001x

Voermans, J. J., Ghisalberti, M., & Ivey, G. N. (2017). The variation of flow and turbulence across the sediment–water interface. *Journal of Fluid Mechanics*, *824*, 413–437. https://doi.org/10.1017/jfm.2017.345

Voermans, J. J., Marco, G., & Ivey, G. N. (2018). A Model for Mass Transport Across the Sediment-Water Interface. *Water Resources Research*, *54*(4), 2799–2812. https://doi.org/10.1002/2017WR022418

Xu, Z., Hu, B. X., & Ye, M. (2018). Numerical modeling and sensitivity analysis of seawater intrusion in a dual-permeability coastal karst aquifer with conduit networks. *Hydrology and Earth System Sciences*, *22*(1), 221–239. https://doi.org/10.5194/hess-22-221-2018

Yadav, D., Wang, J., & Lee, J. (2017). Onset of Darcy-Brinkman Convection in a rotating porous layer induced by purely internal heating. *Journal of Porous Media*, *20*(8), 691–706. https://doi.org/10.1615/JPorMedia.v20.i8.20

Younes, A., Makradi, A., Zidane, A., Shao, Q., & Bouhala, L. (2014). A combination of Crouzeix-Raviart, Discontinuous Galerkin and MPFA methods for buoyancy-driven flows. *International Journal of Numerical Methods for Heat & Fluid Flow*, *24*(3), 735–759. https://doi.org/10.1108/HFF-07-2012-0156